Fault-Tolerant Flight Control
Using One Aerodynamic Control Surface

Raghu Venkataraman* and Peter Seiler†
University of Minnesota, Minneapolis, Minnesota 55455

This paper considers a statically stable unmanned aircraft that is equipped with only two aerodynamic control surfaces (called elevons) and one tractor-type propeller. A fault in either of the elevons must, therefore, be managed using only the other elevon and the throttle. Since the fault results in an under-actuated aircraft, the reconfiguration possibilities are limited. This paper proposes a strategy of using the throttle for total energy control and the single operable elevon for lateral control. This paper then develops a fault-tolerant controller based on this strategy and demonstrates, via multiple flight tests, the autonomous guidance and final approach of this unmanned aircraft in the presence of a stuck elevon fault. The results indicate that it may be possible to control other aerial bodies, including larger aircraft, using one aerodynamic control surface.

Nomenclature

B	=	balance (or difference) of the kinetic and potential energies, J
d	=	disturbance at plant input or output
E	=	total (or sum) of the kinetic and potential energies, J
F_L	=	lower linear fractional transform
g	=	acceleration due to gravity, m/s^2
G	=	linear plant model
h	=	altitude above ground level, m
K	=	controller or kinetic energy (J)
L	=	loop transfer function
m	=	mass, kg
p_N, p_E, p_D	=	position of the aircraft in local North-East-Down frame, m
p, q, r	=	angular velocity in the body axes, rad/s
S	=	sensitivity function

---
*Graduate Student, Department of Aerospace Engineering and Mechanics; venka085@umn.edu.
†Associate Professor, Department of Aerospace Engineering and Mechanics; seile017@umn.edu.

T	=	mixed energy (J) or complementary sensitivity function
u, v, w	=	airspeed in the body axes, m/s
w_b	=	balance energy weight
U	=	potential energy, J
V	=	total airspeed, m/s
W	=	weighting function
δ_a	=	aileron, rad
δ_e	=	elevator, rad
δ_l	=	left elevon, rad
δ_r	=	right elevon, rad
δ_t	=	throttle
ϕ, θ, ψ	=	Euler angles, rad
τ	=	time delay, s
ω_n	=	natural frequency, rad/s
ζ	=	damping ratio

Subscripts

c	=	actuator commands
cmd	=	reference commands
i	=	input
lat	=	lateral-directional dynamics
lon	=	longitudinal dynamics
o	=	output

I. Introduction

Fault management is one of several technical challenges facing the widespread use of small unmanned aircraft systems (UAS). While each component of a small UAS can fail in a number of different ways, some failure modes are more likely to occur and are more severe in consequence than others [1]. The aerodynamic control surfaces of a fixed-wing UAS perform the safety-critical functions of stabilizing and controlling the aircraft. Failures in one or more of these surfaces, or the actuators controlling them, pose acute safety risks to the UAS and to the surrounding environment. These safety risks may be mitigated by using a *fault-tolerant* control system that reallocates the remaining operable control surfaces and/or propulsive devices to provide adequate control authority to the handicapped aircraft.

Several textbooks address the general subject of fault-tolerant control (FTC) [2–5] and others address the specific subject of fault-tolerant *flight* control [6, 7]. The latter has received considerable attention over the years as demonstrated by the literature surveys of Steinberg [8] and Zhang and Jiang [9]. Common scenarios include actuator/control surface failures, sensor failures, loss of thrust, loss of lifting surfaces, and structural damage. The fault-tolerant flight control design methods that are reported in the literature include multiple model [10, 11], adaptive control [12–17], receding horizon control (RHC) [18–21], H_∞ optimal control [22, 23], gain scheduled/LPV control [24, 25], and nonlinear dynamic inversion (NDI) [26–30]. In addition, indirect adaptive control has been enabled by the advances made in real-time parameter identification [13, 19, 31–34]. The identified plant parameters are then used adaptively in other control techniques, such as RHC [19, 21] and NDI [28, 30]. All of these FTC techniques involve either replacing or adapting the baseline controller after the occurrence of one or more faults. On the other hand, retrofit fault-tolerant controllers are designed to add-on to, and operate alongside, the baseline controller [20, 35]. In contrast to the model-based FTC techniques discussed thus far, Handelman and Stengel [36] propose a data-driven, rule-based expert system approach to solving FTC by drawing on concepts from artificial intelligence. Some research efforts have included flight demonstrations of FTC on fixed-wing aircraft in the presence of actuator, thrust, and airframe failures [10, 11, 15–17, 19, 20, 28, 29]. In addition, a detailed literature review of the fault-tolerant control strategies used on flying wing UAS is given in [37]. Various forms of adaptive control have been applied for this purpose [38, 39].

The literature cited thus far covers various types of aircraft equipped with different numbers of control surfaces. The novelty of this paper lies in the fact that it considers a UAS that is equipped with only two aerodynamic control surfaces (called elevons) and one tractor-type propeller (Fig. 1a). A fault in either of the elevons of this UAS must, therefore, be managed using only the other elevon and the throttle. An important assumption in this regard is that the aircraft is statically stable. The possibility of automatically controlling a UAS using one aerodynamic control surface was originally demonstrated in [40, 41] on a large fixed-wing UAS, but these demonstrations were limited to straight and level flight and banked turns. The possibility of landing a UAS using one aerodynamic control surface was originally demonstrated in [42], but this was performed by a skilled human pilot. This paper addresses both of these shortcomings by demonstrating the autonomous guidance and final approach of a UAS using only one elevon and the throttle.

The UAS considered in this paper is one among several that are equipped with only two elevons and one motor*. Almost all of them are low-cost and are used for aerial photography. Figure 1b shows an illustrative mission wherein the aircraft nominally flies a lawnmower-like pattern (dashed ground track). When a fault occurs in one of the elevons, the mission is aborted and the aircraft is directed to fly to a landing zone (solid ground track). Depending on which elevon has failed, it may be preferable to bank in one direction, as opposed to the other. This may in turn make some landing zones more accessible than others, e.g. the easterly landing zone in Fig. 1b.

This paper develops a fault-tolerant controller for the scenario described above and demonstrates, via multiple

---

*Other examples include the Agribotix Hornet, Trimble UX5, senseFly eBee, and RoboFlight RF1.

flight tests, the autonomous guidance and final approach of this UAS in the presence of a stuck elevon fault. Section II presents the aircraft model, the control law, and explains the challenges of single surface control. Section III develops the fault-tolerant controller based on the strategy of using the throttle for total energy control and the single operable elevon for lateral control. While this strategy sacrifices longitudinal tracking performance, the fault-tolerant control design ensures that the phugoid and the short period modes have favorable properties. In particular, the total energy controller uses a new measure called the mixed energy to increase the closed-loop damping ratio of the phugoid mode. Further, H_∞ optimization is leveraged to ensure that the single operable elevon does not excite the short period mode. Section IV compares the H_∞ single surface controller to a proportional-integral-derivative (PID) design and assesses the robustness of the fault-tolerant controller. Section V explains the scope of the flight tests, examines one particular flight in detail, and presents a comparative analysis of all the flight tests. Section VI presents the conclusions of this work.
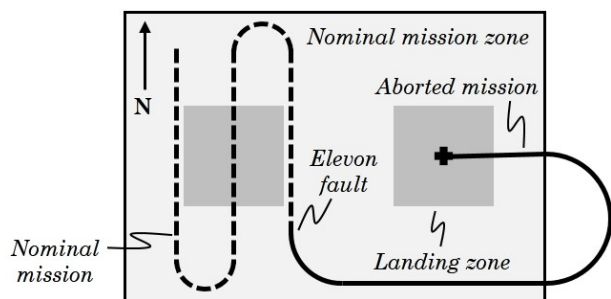
II. Preliminaries

A. Aircraft Model

The aircraft is called the Vireo and is comprised only of a wing and a fuselage (Fig. 1a). This aircraft was originally built by Sentera, LLC and is currently maintained and operated by the University of Minnesota. The fully integrated aircraft has a gross mass of 1.28 kg, a wing span of 0.97 m, and a fuselage length of 0.52 m. Control is provided via a pair of independently actuated elevons and a tractor-type fixed-pitch propeller. Since the aircraft does not have a rudder, directional control is achieved indirectly via lateral control. Sensing is provided via an inertial measurement unit, a global positioning system receiver, a magnetometer, and a pitot-static system. A flight computer implements the software for sensing, navigation, guidance, control, telemetry, and data logging [43].


(a) The aircraft has two elevons and a motor. (b) Illustration of an aerial photography mission.

Fig. 1 The UAS is typically used for aerial photography.

A nonlinear, six degrees-of-freedom model of this aircraft is developed using physics-based first-principles [43]. The geometric, inertial, propulsive, and aerodynamic properties of this aircraft are modeled using a combination of computational and experimental methods. In particular, the stability and control derivatives are initially estimated

using the vortex-lattice method and subsequently updated using system identification flight experiments [43]. Since this aircraft is assumed to be rigid, the pertinent states are the Euler angles (ϕ, θ, ψ), the angular velocity in the body axes (p, q, r), the airspeed in the body axes (u, v, w), and the position of the aircraft in a local North-East-Down frame (p_N, p_E, p_D) (see Fig. 2). The nonlinear equations of motion of rigid, fixed-wing aircraft are documented in several textbooks [44, 45] and are thus not repeated here. In order to design controllers, these equations are linearized about a steady, wings-level, constant altitude flight condition, at a cruise airspeed of 15.4 m/s.
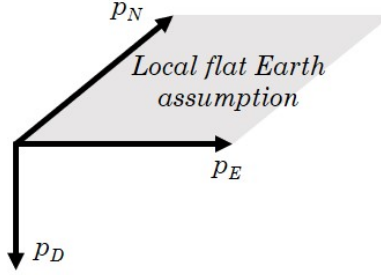
Fig. 2   The local North-East-Down reference frame.

The throttle δ_t is normalized to the interval $[0, 1]$. The left δ_l and the right δ_r elevons can each attain a physical deflection range of $[-30, +20]\,°$, where positive values correspond to trailing-edge down deflections. As such, each elevon excites both the longitudinal and the lateral-directional dynamics. Therefore, for modeling convenience, these dynamics are decoupled by expressing the elevons in terms of the traditional elevator δ_e and the aileron δ_a via the relations $\delta_l = \delta_e - \delta_a$ and $\delta_r = \delta_e + \delta_a$. The linearized equations of motion are described by:

$$
\begin{aligned}
\mathbf{x}_\star &= \mathbf{A}_\star \mathbf{x}_\star + \mathbf{B}_\star \mathbf{u}_\star, \\
\mathbf{y}_\star &= \mathbf{C}_\star \mathbf{x}_\star + \mathbf{D}_\star \mathbf{u}_\star,
\end{aligned}
\tag{1}
$$

where $\mathbf{x}_\star$, $\mathbf{u}_\star$, and $\mathbf{y}_\star$ represent perturbations in the state, input, and output vectors, respectively, from the equilibrium flight condition described earlier. The subscript $\star$ is replaced with either *lon* or *lat* as explained next. The longitudinal dynamics G_{lon} use: $\mathbf{x_{lon}} = [u, w, q, \theta, p_D]^T$, $\mathbf{u_{lon}} = [\delta_t, \delta_e]^T$, and $\mathbf{y_{lon}} = [V, q, \theta, h]^T$. Note that $V = \sqrt{u^2 + v^2 + w^2}$ is the total airspeed and $h = -p_D$ is the altitude above ground level (AGL). The lateral-directional dynamics G_{lat} use: $\mathbf{x_{lat}} = [v, p, r, \phi]^T$, $\mathbf{u_{lat}} = \delta_a$, and $\mathbf{y_{lat}} = [\phi, p]^T$. The Appendix provides the state-space matrices of G_{lon} and G_{lat}. The states p_N, p_E, and ψ are used to design the guidance law. They are omitted here since this paper focuses on the control design. Table 1 provides the damping ratio ζ and the natural frequency ω_n of the aircraft dynamic modes. Note that the aircraft is statically stable and has a damping ratio of $\zeta = 0.39$ for the short period mode. This property is key to eventually controlling it using only one elevon and the throttle.

Table 1   The open-loop modal characteristics of the aircraft.

Mode	ζ	ω_n (rad/s)
Short period	0.39	14.5
Phugoid	0.094	0.87
Roll subsidence	1	12
Dutch roll	0.13	4.1
Spiral	1	0.12

The dynamics of the throttle and the elevon actuators are respectively given by:

$$G_t(s) = \frac{\omega_t}{s + \omega_t} \quad \text{and} \quad G_a(s) = \frac{\omega_a^2}{s^2 + 2\zeta_a\omega_a s + \omega_a^2}. \tag{2}$$

The model parameters are estimated using system identification experiments [43] as: $\omega_t = 6.28$ rad/s, $\zeta_a = 0.77$, and $\omega_a = 62.8$ rad/s. The experiments also quantify the closed-loop time delay as $\tau_f = 0.05$ s, which encompasses delays in the actuators, the flight computer, and the sensors. For the purpose of control design, all of this delay is grouped at the input to the actuators and modeled using Padé approximations. The delay-free approximations of $G_t e^{-\tau_f s}$ and $G_a e^{-\tau_f s}$ are denoted by G_t^P and G_a^L, respectively, and are described in the Appendix.

B. Guidance Law

The guidance law provides the reference commands $(V_{cmd}, h_{cmd}, \phi_{cmd})$ to the control law. The UAS operator directly specifies V_{cmd} and h_{cmd} during the cruise phase and h_{cmd} is varied along the glideslope during the landing phase. The nonlinear guidance law developed by Park et al. [46] is used to compute ϕ_{cmd}. In particular, the law uses the ground speed and the ground track of the aircraft to calculate the lateral acceleration command $a_{y,cmd}$ [46]. The bank angle command is then computed as $\phi_{cmd} = \tan^{-1}(a_{y,cmd}/g)$. When following a straight line path, the guidance law approximates a proportional-derivative controller on the cross-track error. In addition, the guidance law projects an imaginary point, located at some distance in front ot the aircraft, onto the upcoming flight path. This provides it with an element of anticipation for the tight tracking of curved paths. The reader is referred to [46] for the details of the guidance law, a Lyapunov-based proof of its asymptotic stability, and the flight test results demonstrating its efficacy.

C. Control Law

The linear time-invariant (LTI) models G_{lon}, G_{lat}, G_t^P, and G_a^L are used to design the nominal controller (NC) and the fault-tolerant controller (FTC), which together makeup the control law shown in Fig. 3. Both the NC and the FTC use the reference commands $(V_{cmd}, h_{cmd}, \phi_{cmd})$ and the outputs (y_{lon}, y_{lat}) to compute the actuator commands $(\delta_{tc}, \delta_{lc}, \delta_{rc})$. When a fault occurs, the control law switches from the NC to the FTC. The NC is a classical, cascaded-loop design that consists of total energy, pitch attitude, and roll attitude controllers. The pitch attitude is tracked using a

proportional-integral (PI) controller and the pitch rate is damped using a proportional gain. The roll channel is setup similarly. This paper focuses on the FTC and the reader is referred to Chapter 4 of [43] for additional details on the NC. Further, this paper does not consider the issue of stability when switching from NC to FTC. The reader is referred to articles on switching control [47] and supervisory fault-tolerant control [48] for additional details.
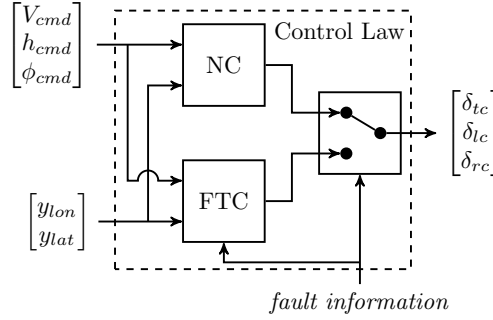
Fig. 3   The control law consists of the nominal controller (NC) and the fault-tolerant controller (FTC).

The control law described above is often referred to in the literature as the multiple model approach. This is because NC and FTC are designed using two different, but related, aircraft models. This approach requires an explicit fault diagnosis algorithm since there is a discrete switch in the operational controller. The flight demonstrations presented in Section V do not implement a fault diagnosis algorithm. Rather, the fault information is made available at runtime. The reader is referred to Chapter 6 of [43] for a detailed discussion of the maximum allowable fault detection delay, two candidate fault diagnosis algorithms, and their performance with flight data.

The approach described above contrasts with adaptive control approaches, wherein the controller parameters are varied in response to the fault, thus circumventing the need for explicit fault diagnosis. The multiple model approach is chosen for this particular problem because NC and FTC have different feedback architectures. In particular, the FTC does not track the commanded pitch attitude and does not damp the pitch rate. In addition, the FTC introduces mixing within the total energy controller. These architecture changes are required because the aircraft becomes under-actuated after the fault and all the nominal control objectives cannot be satisfied using only the throttle and one elevon. These challenges are explained in the next subsection.

D. Fault-Tolerant Control Strategy

The longitudinal and the lateral-directional dynamics are not separable when one of the elevons is stuck, because the operable elevon excites motion in both axes. The fault-tolerant flight controller is thus considered using the full, coupled linear model with the state vector $\mathbf{x} = [\phi, \theta, p, q, r, u, v, w, p_D]^T$. For the purpose of illustration, consider the right elevon to be stuck at trim. The input of this model is then $\mathbf{u} = [\delta_t, \delta_l]^T$. Further, consider the output $\mathbf{y} = [V, h, \phi, \theta, p, q, r]^T$. Let G_f denote the model (for a stuck right elevon) obtained using the aforementioned state, input, and output. The

Appendix provides the state-space matrices (A, B, C, D) of G_f. At this stage, the number of outputs and states far exceed the number of available inputs. Since, the fault-tolerant flight controller can reasonably track only a limited number of outputs, the following questions are posed to guide its design. (1) Are all the states controllable and observable, and to what extent? (2) What outputs are the most impacted by the available inputs? (3) Are some outputs more important to control than others? If so, how should they be prioritized? (4) What model properties can help mitigate the impact of uncontrolled outputs? The answers are obtained from flight dynamics [44, 45] and the concept of input-output controllability [49].

To answer the first question, the state p_D is truncated from G_f to make A Hurwitz. The controllability $\mathbf{W_c}$ and the observability $\mathbf{W_o}$ gramians are both positive definite, indicating that all the states are controllable and observable. The maximum and minimum singular values of $\mathbf{W_c}$ are 1588 and 9, indicating that some states are weakly controllable. When $\mathbf{W_c}$ is recomputed with only the throttle input, its diagonal entries indicate that u is the most controllable state and the lateral-directional states are the least controllable. On the other hand, when $\mathbf{W_c}$ is recomputed with only the elevon input, its diagonal entries indicate that (p, q, u, v, w) are highly controllable.

To answer the second question, note that δ_t has the most impact on V and h. The fault-tolerant controller thus controls the total energy using δ_t. On the other hand, δ_l has roughly equal impact on p and q, and slightly more impact on ϕ than θ. Since (ϕ, p) and (θ, q) are not independently controllable, the third question needs to be answered. Specifically, given that the final goal is to perform an autonomous landing, a given landing zone can be reached only if the aircraft has the ability to change and maintain course. Thus, roll attitude control (ϕ, p) is of a higher priority.

The throttle is not useful to control θ and q because the thrust line is very close to the center of gravity [43]. Moreover, the throttle actuator bandwidth (1 Hz) is too low to control the short period mode (2.3 Hz). Thus, θ and q are relegated to being uncontrolled outputs, which leads to the fourth and final question. In this regard, the most exploitable model property is the stability of the short period mode ($\zeta = 0.39$; see Table 1). In order to avoid affecting the short period mode damping, the fault-tolerant controller exploits the modal frequency separation, as described next.

Figure 4 shows the Bode diagrams of the open-loop plant from the left elevon δ_l to the controlled outputs (ϕ, p) and the uncontrolled outputs (θ, q). The figure indicates that the phugoid mode (0.87 rad/s) and the short period mode (14.5 rad/s) straddle the dutch roll mode (4.1 rad/s). This frequency separation is exploited by controlling ϕ and p up to a bandwidth that is no greater than 4 rad/s, thereby ensuring that the left elevon does not inadvertently excite the short period mode. Further, owing to the large low-frequency gain from δ_l to ϕ, a given roll attitude command can be achieved using a very small change to the steady-state value of δ_l. This ensures that the steady-state pitch angle, which defines the trim airspeed, is relatively unaltered by the fault-tolerant roll attitude controller. On the other hand, the phugoid mode is within the intended bandwidth of the fault-tolerant controller, and will thus get excited by the left elevon. This problem is managed by the total energy controller, wherein some modifications help increase the phugoid mode damping ratio. Finally, two points are noted with regard to the strategy developed thus far. First, it is dependent on

the static stability of the aircraft. For aircraft that have reduced or marginal static stability, a strategy that also considers the longitudinal stability will be required. Second, there may be other competing strategies that allow one to achieve the final goals, e.g. one could combine the throttle and the elevon for both roll attitude control and total energy control.
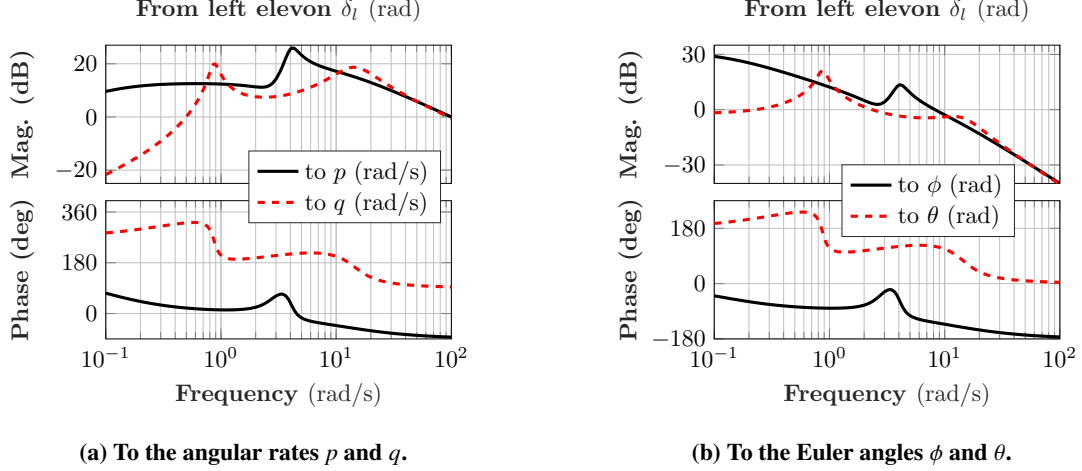

(a) To the angular rates p and q.

(b) To the Euler angles ϕ and θ.

Fig. 4   The Bode diagrams of the open-loop plant.

III. Fault-Tolerant Control Design

The fault-tolerant controller consists of a *total energy controller* $\bar{K}_{TECS}$ that uses the throttle to control (V, h) and a *single surface controller* K_S that uses the elevon to control (ϕ, p). The design of each is taken up one by one.

A. Total Energy Controller

The total energy controller poses the problem of controlling the altitude h and the airspeed V of the aircraft into a problem of controlling its potential and kinetic energies. Although it was originally introduced by Lambregts in 1983 [50, 51], this paper uses the alternative formulation given in [52]. The commanded and the actual potential energies are:

$$U_{cmd} = U_0 + mgh_{cmd} \quad \text{and} \quad U = U_0 + mgh, \tag{3}$$

where U_0 is the potential energy at any reference altitude. Similarly, the commanded and the current kinetic energies are:

$$K_{cmd} = \frac{1}{2}mV_{cmd}^2 \quad \text{and} \quad K = \frac{1}{2}mV^2. \tag{4}$$

The controlled variables are the sum (or the total)

$$E = K + U \tag{5}$$

and the difference (or the balance)

$$B = K - U \tag{6}$$

of the two energies. When both the elevons are functional, the throttle tracks the commanded total energy

$$E_{cmd} = K_{cmd} + U_{cmd} \tag{7}$$

and the elevator (elevons deflected symmetrically) tracks the commanded balance energy

$$B_{cmd} = K_{cmd} - U_{cmd}. \tag{8}$$

This approach is no longer tenable when one of the elevons fails because, as per Section II.D, the operable elevon is prioritized for lateral control. It is insufficient to merely track the commanded total energy using the throttle because the exchange between the two forms of energy is not actively regulated. Thus, even if the total energy is constant throughout a maneuver, an (undesired) exchange between the kinetic and the potential energies is possible, as in the phugoid mode [44]. This is of particular concern for the Vireo since its phugoid mode is lightly damped ($\zeta = 0.094$; see Table 1).

In order to alleviate this problem, $\bar{K}_{TECS}$ is designed using the feedback structure shown in Fig. 5, where G_{lon} models the longitudinal dynamics, G_t^P models the throttle actuator dynamics (Section II.A), and δV and δh denote disturbances in V and h, respectively. The energy calculation block computes the total energy error

$$\Delta E = E_{cmd} - E \tag{9}$$

and the balance energy error

$$\Delta B = B_{cmd} - B. \tag{10}$$

In addition, a new measure called the *mixed energy* error is defined as

$$\Delta T = \Delta E + w_b \Delta B, \tag{11}$$

where the weight $w_b \in [-1, +1]$. K_{TE} implements a PI controller to drive ΔT to zero using the throttle command δ_{tc}. Given this architecture, the design of $\bar{K}_{TECS}$ boils down to selecting the gains of K_{TE} and the weight w_b.

The total energy controller is nonlinear because of the inclusion of V^2 in the kinetic energy term. In order to apply linear control design techniques, the energy calculation block is linearized about the same flight condition as G_{lon}. In this regard, note that K_{TE} appears in both the nominal and the fault-tolerant controllers, whereas w_b appears only in the fault-tolerant controller. The nominal controller uses a separate PI controller to regulate ΔB by issuing elevator

10
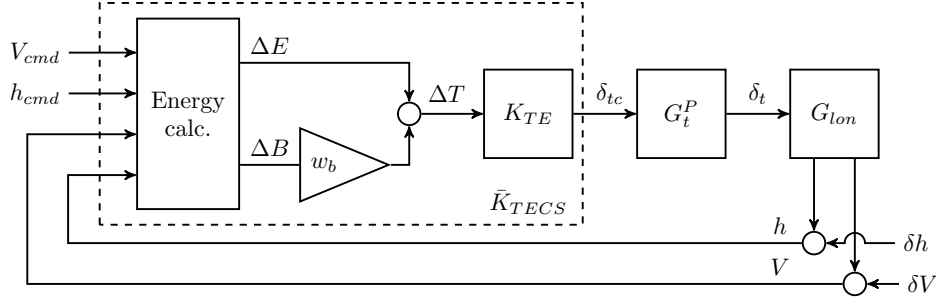
Fig. 5 The feedback structure used to design $\bar{K}_{TECS}$.

commands. K_{TE} is selected during the nominal controller design process, the details of which can be found in Chapter 4 of [43]. The gains of K_{TE} are initially tuned using the root locus design technique and then iteratively updated using flight tests, finally resulting in

$$K_{TE} = 6 \times 10^{-4} + \frac{4 \times 10^{-5}}{s}. \tag{12}$$

This value is unchanged even after the onset of a control surface fault. The tolerance to the fault is provided through the weight w_b, as explained next.

Once K_{TE} is fixed at a particular value, varying w_b almost exclusively affects the phugoid mode damping ratio. In particular, Fig. 6 shows a root locus plot of the closed-loop phugoid mode as a function of w_b. Selecting $w_b = 0$ leads to a negligible change in the pole from its open-loop location (+) because K_{TE} only drives ΔE to zero. Selecting $w_b < 0$ is not beneficial because it decreases ζ. Thus, in order to increase the phugoid mode damping ratio, w_b should be selected in the interval $(0, 1]$. Although selecting a large positive value for w_b increases the phugoid mode damping, it comes at the expense of decreased altitude tracking performance. For example, selecting $w_b = 1$ results in $\zeta \approx 0.18$, but implies that

$$\Delta T = \Delta E + \Delta B = 2\left(K_{cmd} - K\right). \tag{13}$$

In this case, the $\bar{K}_{TECS}$ does not respond to altitude reference commands.

A flight test is conducted wherein w_b is varied in the interval $(0, 1]$. (See Chapter 7 of [43] for details.) It is determined that $w_b = 0.4$ offers a good trade-off between the phugoid mode damping ($\zeta = 0.13$) and the altitude tracking performance. This trade-off is visualized using the cross-channel output sensitivity functions $\delta V \rightarrow h$ and $\delta h \rightarrow V$ associated with the closed-loop shown in Fig. 5. Figure 7 shows the Bode diagrams of these sensitivities for $w_b = \{0, 0.4\}$. Both the sensitivities exhibit bandpass behavior near the phugoid mode (0.87 rad/s) due to the coupling between V and h. However, the peak sensitivity in the $\delta h \rightarrow V$ channel is 7 dB lower for $w_b = 0.4$ due to the increased phugoid mode damping. This comes at the price of increased sensitivity in the $\delta V \rightarrow h$ channel at low and high frequencies. Thus, even if the phugoid mode is well-damped, a steady-state error in V will produce a steady-state error in h. There does not appear to be an easy way around this constraint. Nevertheless, the flight tests (Section V) show that

11
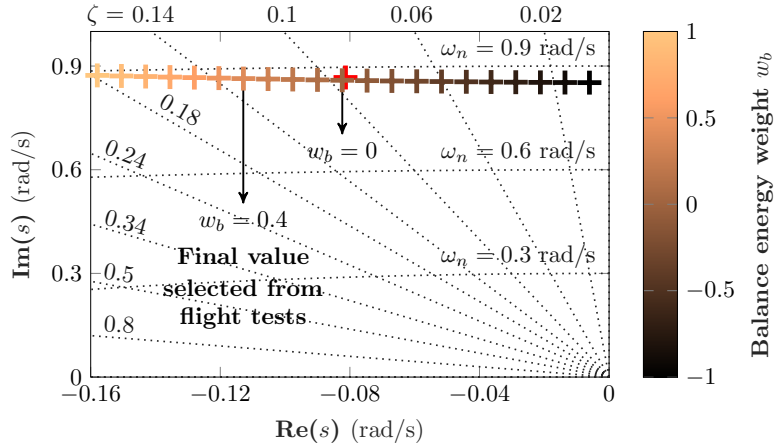
Fig. 6   Root locus plot of the closed-loop phugoid mode as a function of w_b.

this is, on the whole, a price worth paying. Finally, while this section outlines one particular method of choosing K_{TE} and w_b, there may be others, e.g. iteratively choosing the gains so as to yield higher phugoid mode damping ratios with smaller increases in the sensitivities.
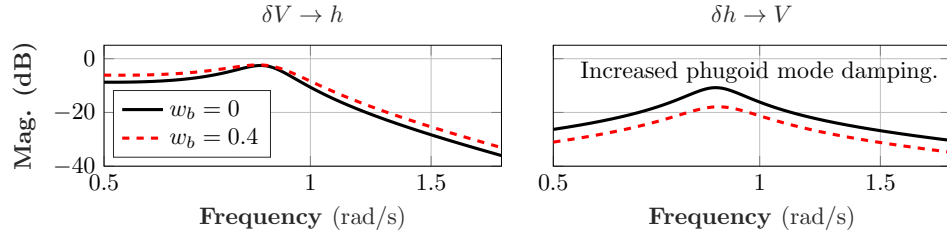

Fig. 7   The Bode diagrams of the output sensitivity functions $\delta V \rightarrow h$ and $\delta h \rightarrow V$.

## B. Single Surface Controller

Section II.D put forth the strategy of using the operable elevon for lateral control. The main component of the single surface controller K_S is thus a roll attitude controller K_A, as shown in Fig. 8. Depending on the fault information received, the switch sends the aileron command δ_{ac} generated by K_A to either the left or the right elevon. Figure 8 shows an instance of the switch for the case of a stuck right elevon. To understand the rationale behind this architecture, first note that $\delta_{lc} = \delta_{ec} - \delta_{ac}$ and $\delta_{rc} = \delta_{ec} + \delta_{ac}$, and then note that the elevator command δ_{ec} is zero.

K_A is designed using the feedback structure shown in Fig. 9, where G_{lat} models the lateral-directional dynamics, G_a^L models the actuator dynamics, and $G := G_{lat} G_a^L$. For aircraft that have reduced or marginal static stability, one may also need to consider the longitudinal aircraft dynamics G_{lon} in the synthesis. The input $\tilde{d}_1$ and output $\tilde{d}_2 = [\delta\phi, \delta p]^T$ disturbances are used to define the following sensitivities, which are used later to analyze the closed-loop performance and robustness. S_i is the transfer function $\tilde{d}_1 \rightarrow \delta_{ac}$, S_o is the transfer function $\tilde{d}_2 \rightarrow [\phi_n, p_n]^T$, T_i is the transfer
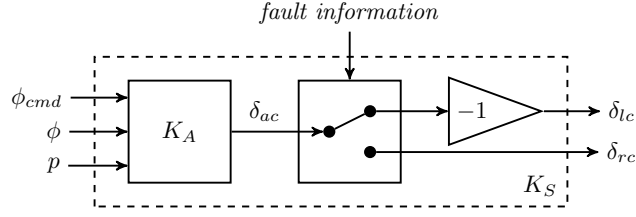
Fig. 8   The architecture of the single surface controller K_S.

function $\tilde{d}_1 \rightarrow u$, and T_o is the transfer function $\tilde{d}_2 \rightarrow [\phi, p]^T$. The disturbance sensitivity $GS_i \, (= S_o G)$ is the transfer function $\tilde{d}_1 \rightarrow [\phi, p]^T$. Further, note that K_A is partitioned as $\begin{bmatrix} K_{Ar} & K_{Ay} \end{bmatrix}$, where K_{Ar} only includes ϕ_{cmd} and K_{Ay} only includes $[\phi_n, p_n]^T$. This is used to define the control sensitivity $K_{Ay}S_o \, (= S_i K_{Ay})$ as the transfer function $\tilde{d}_2 \rightarrow u$.
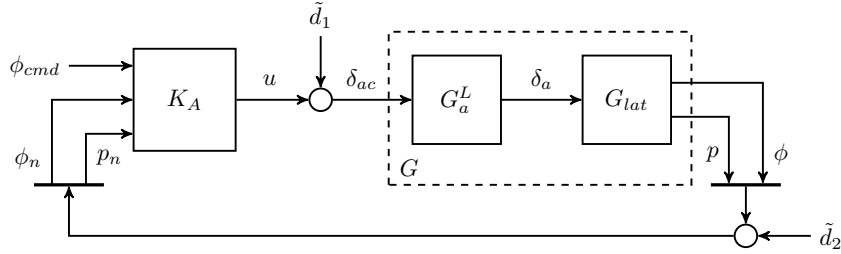

Fig. 9   The feedback structure used to design K_A.

K_A is designed using H_∞ synthesis [49] and is guided by the following control design objectives. K_A should: (1) track a roll angle command ϕ_{cmd} with a bandwidth of 1.5 rad/s, (2) provide a closed-loop dutch roll mode damping ratio of at least 0.3, (3) ensure zero steady-state error in tracking ϕ_{cmd}, (4) penalize excessive control effort in δ_{ac} above 2.7 rad/s, and (5) be robust to disturbances at the plant input $\tilde{d}_1$ and output $\tilde{d}_2$. The first objective ensures that the bandwidth in the $\phi_{cmd} \rightarrow \phi$ channel is thrice the natural frequency of the cross-track error dynamics [43]. The second objective ensures that dutch roll mode satisfies the minimum requirement for Level-1 flying quality [45]. The fourth objective ensures that the single elevon does not excite the short period mode. The fifth objective ensures that the controller meets the minimum desired robustness margins, as explained in Section IV.B.

The design objectives are codified using weights, which are interconnected with $G_{lat} G_a^L$ to form the generalized plant shown in Fig. 10. The generalized plant P consists of all the systems shown in Fig. 10, except for the as-of-yet undetermined controller $\bar{K}_A$, enclosed by the dashed box. Although the synthesis results in $\bar{K}_A$, the final controller of interest is K_A, which comprises $\bar{K}_A$, the integrator $\frac{1}{s}$, and the sum junction, as indicated by the shaded box. The integrator ensures zero-steady state error in ϕ. P has three generalized disturbance inputs (d_1, d_2, d_3), one control input (u), three generalized error outputs (e_1, e_2, e_3), and three measurement outputs $(e_\phi$, its integral, $p_n)$.

The weight W_1 relates disturbances at the plant input $\tilde{d}_1$, e.g. atmospheric turbulence, to its normalized counterpart d_1. The weight W_2 relates disturbances at the plant output $\tilde{d}_2$, e.g. sensor noise, to its normalized counterpart d_2. W_1
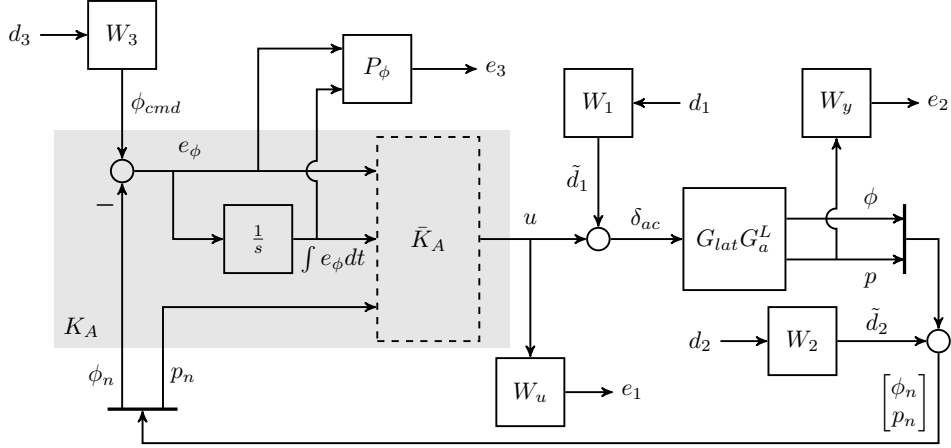
Fig. 10   The generalized plant for the single surface controller.

and W_2 together codify the fifth objective and control the relation between the input and output margins. The weight W_3 relates ϕ_{cmd} to its normalized counterpart d_3. The noisy roll rate p_n is directly fed back to $\bar{K}_A$, whereas the noisy roll angle ϕ_n is first used to compute the tracking error $e_\phi = \phi_{cmd} - \phi_n$, which is then fed to $\bar{K}_A$ along with its integral. The weight P_ϕ penalizes large tracking errors. An appropriate penalty on e_ϕ codifies the first objective, while any non-zero penalty on its integral codifies the third objective. The weight W_y penalizes large roll rates and codifies the second objective. Finally, the weight W_u penalizes excessive control effort and codifies the fourth objective.

The weighted closed-loop $F_L\left(P, \bar{K}_A\right)$ has the inputs (d_1, d_2, d_3) and outputs (e_1, e_2, e_3). The synthesis involves a search for $\bar{K}_A$ such that $\left\|F_L\left(P, \bar{K}_A\right)\right\|$ is minimized. This is an iterative process that involves weight selection and tuning. Table 2 lists the final values of all the weights, along with their interpretations. The performance of the resultant controller is evaluated using: the nine transfer functions that compose $F_L\left(P, \bar{K}_A\right)$, the input and output sensitivities, the closed-loop step response, the damping ratio of the closed-loop dutch roll mode, and the robustness margins.

**Table 2   The final weights selected for the H_∞ synthesis.**

Weight	Final value	Weight interpretation
W_1	$6\,(\pi/180)$	Aileron disturbance at plant input.
W_2	$\begin{bmatrix} 5 & 0 \\ 0 & 50 \end{bmatrix}(\pi/180)$	Disturbance at the plant output $[\phi, p]^T$.
W_3	$150\,(\pi/180)$	Roll angle command.
P_ϕ	$\begin{bmatrix} 0.4 & 1.6 \end{bmatrix}$	Inverse of the desired sensitivity function from ϕ_{cmd} to e_ϕ.
W_y	$(1/250)\,(180/\pi)$	Inverse of the desired roll rate.
W_u	$\frac{60.31(s+3778)(s+38.73)(s+8.762)(s+0.897)}{(s+2857)(s+872.2)(s+28.08)(s+1.887)}$	Inverse of the desired aileron commands across frequency.

Let S_ϕ and $\bar{S}_\phi$ denote the sensitivity function $\phi_{cmd} \to e_\phi$ and its upper bound, respectively. In order to select P_ϕ,

the bound is first chosen as $\bar{S}_\phi = \frac{k_\phi s}{s+p_\phi}$. This choice has zero low-frequency gain and thus satisfies the third control design objective. Given this bound, e_ϕ should be weighted using

$$\bar{S}_\phi^{-1} = k_\phi^{-1} + p_\phi k_\phi^{-1} s^{-1}. \tag{14}$$

However, since the generalized plant (Fig. 10) contains an integrator, P_ϕ is simply set equal to $\begin{bmatrix} k_\phi^{-1} & p_\phi k_\phi^{-1} \end{bmatrix}$. The pole p_ϕ is selected as 4 rad/s for good tracking performance. This is close to the dutch roll mode (4.1 rad/s) but is sufficiently lower than the short period mode (14.5 rad/s). The gain k_ϕ $(= \|\bar{S}_\phi\|)$ is selected as 8 dB for good robustness. Figure 11a shows that S_ϕ, which is bounded by $\bar{S}_\phi$, has zero low-frequency gain (zero steady-state error), a peak gain of 2.4 dB at 6.9 rad/s (indicates good robustness), and a bandwidth of 1.5 rad/s (satisfies first control design objective).

(a) The sensitivity S_ϕ and its bound $\bar{S}_\phi$.

(b) The control effort weight W_u.
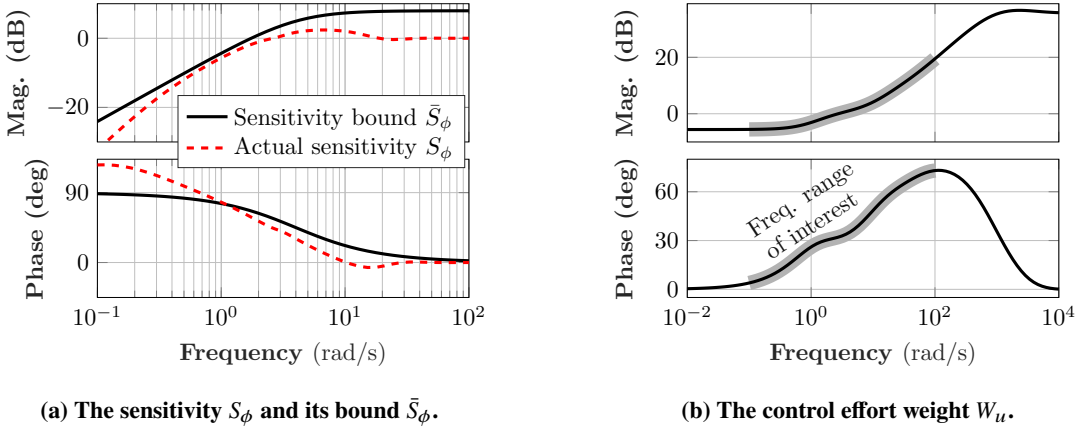
Fig. 11   The Bode diagrams of the sensitivity function and the control effort weight.

The weight W_u (Fig. 11b) is selected to penalize excessive control effort in δ_{ac}. Thus, it has a small low-frequency gain (-5.6 dB), a large high frequency gain (35.6 dB), and crosses 0 dB at 2.7 rad/s as per the fourth control design objective. The magnitude of W_u at a given frequency may be interpreted as the inverse of the desired aileron command at that frequency. For example, the desired δ_{ac} at the actuator bandwidth (57 rad/s) is 10° and at high frequencies is 1°. W_u is selected as a fourth-order system (Table 2) to ensure that its gain rapidly increases with frequency. The remaining weights are selected to normalize the 9 transfer functions that compose $F_L(P, \bar{K}_A)$ to a peak gain of around 0 dB. The weights are interpreted using Table 2. For example, the controller should treat a 6° aileron disturbance (W_1) on par with a 5° roll angle disturbance and a 50°/s roll rate disturbance (W_2). Similarly, a 150° roll angle command (W_3) should elicit a peak roll rate on the order of 250°/s (W_y). Although this last scenario is unrealistic, the key point is that the weights specify a rise time of 0.6 s. The closed-loop dutch roll mode damping ratio is 0.3 (Level-1 flying quality).

The H_∞ synthesis is performed using the two Riccati equation approach [53] using Matlab's Robust Control Toolbox. The synthesis takes approximately 2.7 s and results in a fifteenth-order controller. To reduce its computational overhead during implementation, a balanced residualization is performed to obtain an eighth-order controller, whose state-space

matrices are provided in the Appendix. Further, this controller is discretized with a median sample rate of 90 Hz prior to implementation [43].

C. Saturations

The software implementation of the controllers include command saturations. V_{cmd} is saturated in the interval $[13, 18]$ m/s to prevent the aircraft from stalling or overspeeding. Further, $\phi_{cmd} \in [-35, +20]°$ when the right elevon is failed and $\phi_{cmd} \in [-20, +35]°$ when the left elevon is failed. The motivation for using asymmetric bounds for ϕ_{cmd} arises from the preferred pitch direction of the aircraft. When one of the elevons is failed, it is preferred that the aircraft pitches nose-up rather than nose-down so as not to lose altitude. Hence, the larger bound is used for the roll direction that results from a trailing-edge up deflection of the operable elevon. In addition, $\delta_{tc} \in [0, 1]$ and $\delta_{lc,rc} \in [-20, +20]°$.

IV. Analysis

A. Comparison to a PID Controller

The H_∞ single surface controller described thus far is compared to a PID design, which is obtained by taking the K_A block of Fig. 8 as:

$$\delta_{ac} = K_{RT}\,(\phi_{cmd} - \phi) - K_{RD}\,p, \tag{15}$$

where $K_{RT} = -0.29 - \frac{0.0573}{s}$ is a PI roll angle tracker and $K_{RD} = -0.06$ is a roll rate damper. These gains are chosen such that the PID controller satisfies the first three control design objectives. Figure 12 shows the Bode diagrams of the PID ("Design A") and the H_∞ ("Design B") controllers. Their roll angle tracking performances are similar at low frequencies. However, the H_∞ design rolls off above 2.7 rad/s because the control effort weight W_u has its zero crossover at this frequency. At the dutch roll mode (4 rad/s), Design B is more than 3 dB lower than Design A. Similarly, at the short period mode (14.5 rad/s), Design B is more than 9 dB lower than Design A. The roll rate channel of the H_∞ design rolls off above 42 rad/s and thus attenuates sensor noise. While one could also consider a PID controller with roll-off to reject high frequencies, the H_∞ design explicitly allows the controller to be robust to input and output disturbances.

Figure 13a compares Designs A and B using their closed-loop responses to a 30° step command in the roll angle. With Design A, the roll angle exhibits a rise time (from 10% to 90% of the steady-state value) of 1.1 s, a settling time (within 2% of the steady-state value) of 7.1 s, and an overshoot of 9%. With Design B, the roll angle exhibits a rise time of 0.63 s, a settling time of 7.2 s, and an overshoot of 7%. Further, Design B elicits a maximum roll rate of 67°/s compared to the 116°/s seen with Design A. Similarly, Design B elicits a smaller peak aileron command of −5.2°.

The elevon commands issued by the two designs inevitably excite the longitudinal dynamics. Figure 13b quantifies this impact through the largest singular value of the sensitivity function from the lateral disturbances $[\delta\phi, \delta p]^T$ to the longitudinal variables $[\theta, q]^T$. The peak magnitude near the short period mode is 12 dB for Design A and 3.3 dB for

16
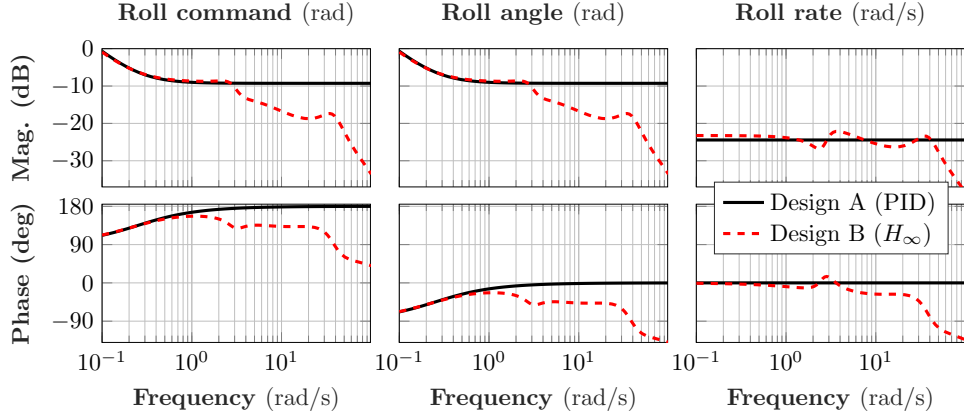
Fig. 12   The Bode diagrams of the two designs of the single surface controller.
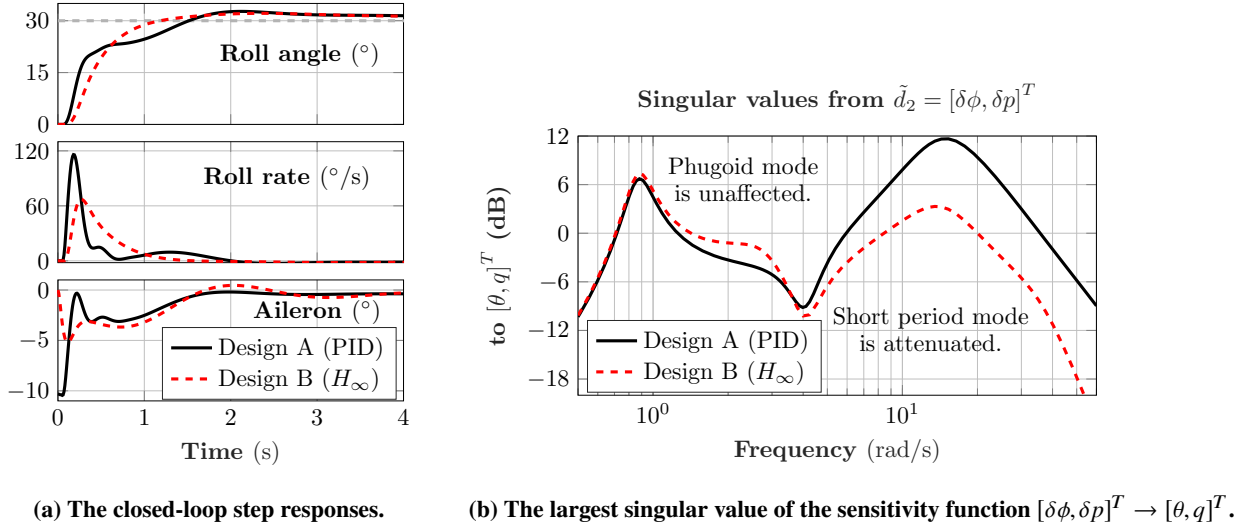
(a) The closed-loop step responses.

(b) The largest singular value of the sensitivity function $[\delta\phi, \delta p]^T \rightarrow [\theta, q]^T$.

Fig. 13   The closed-loop step responses and the largest singular value of $[\delta\phi, \delta p]^T \rightarrow [\theta, q]^T$.

Design B. The short period mode attenuation, which is a consequence of the high gain of W_u above 2.7 rad/s, is useful because (θ, q) are not in feedback with the fault-tolerant controller (Section II.D). The phugoid mode is unaffected because this plot only evaluates the single surface controller. The total energy controller does indeed attenuate the phugoid mode as explained previously in Section III.A.

Finally, Fig. 14 compares Designs A and B using the input and output sensitivity functions defined in Section III.B. The higher robustness of Design B, compared to Design A, is most prominent in the plots of S_o and $K_{Ay}S_o$. The peak gain of the largest singular value of S_o is 7.7 dB for Design B and 10.2 dB for Design A. The largest singular value of S_o is also lower for Design B near the dutch roll mode (4 rad/s) and for all higher frequencies, implying that Design B has better roll angle tracking and roll rate damping. The magnitude of $K_{Ay}S_o$ for Design B is slightly higher than Design A in the range $[1, 3]$ rad/s, but is significantly lower above 4 rad/s, indicating its good noise rejection property.
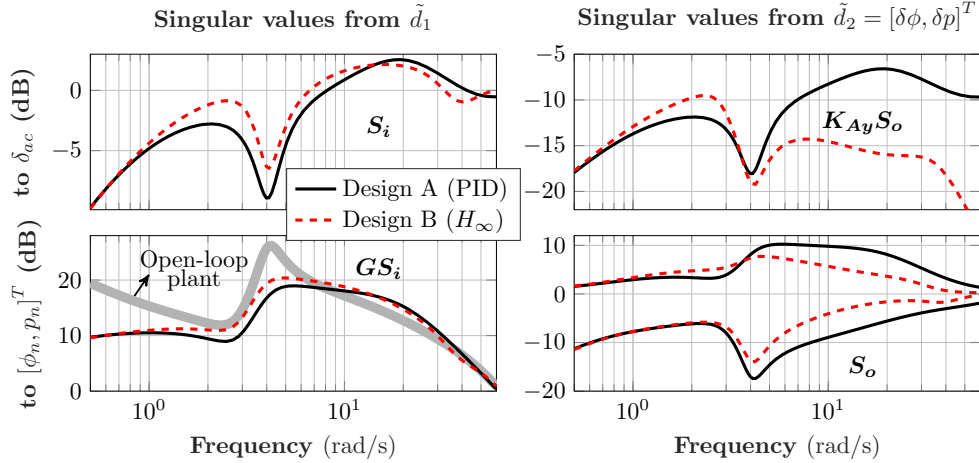
Fig. 14   The singular value diagrams of the input and output sensitivity functions defined in Section III.B.

On the other hand, the higher robustness of Design B is less apparent in the plots of S_i and GS_i. In particular, the peak gain of S_i is 2.12 dB for Design B and 2.52 dB for Design A. The magnitude of S_i for Design B is slightly higher than that of Design A in the range $[1, 14]$ rad/s and slightly lower above 14 rad/s. Similar observations apply to the plot of GS_i, wherein the benefits of Design B are apparent only above 14 rad/s. In comparing the two designs to the open-loop plant, it is clear that feedback control is essential to reducing the impact of input disturbances.

B. Robustness Analysis

The robustness of $\bar{K}_{TECS}$ and K_S are assessed using the disk margins of their respective input-to-plant loop transfer functions L_i (Table 3). The classical gain and phase margins quantify the distance between $L_i(j\omega)$ and the critical point -1 along two specific directions: The negative real axis and the unit circle, respectively. The disk margin provides a direct measure of the minimum distance between L_i and the critical point -1. The disk gain margin β is derived from the largest disk that contains -1, does not intersect L_i, and has a diameter spanning $\left[-\beta, -\beta^{-1}\right]$. The disk phase margin is measured with respect to the point where the disk intersects the unit circle. A good rule of thumb is a disk margin of at least 0.5 on L_i, which corresponds to a minimum disk gain margin of $[0.5, 2]$, a minimum disk phase margin of $\pm 29°$, and a H_∞ norm of 6 dB on the input-to-plant sensitivity function S_i [49]. The crossover frequency of L_i is a good measure of the bandwidth. $\bar{K}_{TECS}$ achieves good disk gain and phase margins, and a high time delay margin owing to the low critical frequency. Both designs of K_S achieve approximately the same bandwidth, which is a result of their similar behavior at low frequencies (Fig. 12). However, when considering $\|S_i\|$ and the disk margins, the H_∞ design is slightly more robust. This design also has a higher time delay margin (0.042 s) than the PID design (0.032 s). All loops achieve the minimum desired disk margins.

Table 3   The disk margins of the loops associated with the components of the fault-tolerant controller.

Controller	Loop transfer function L_i	Crossover (rad/s)	$\lVert S_i \rVert$ (dB)	Disk gain margin $(-)$	Disk phase margin $(°)$	Critical freq. (rad/s)
Total energy controller $\bar{K}_{TECS}$	Break loop at δ_{tc} in Fig. 5	0.062	2.87	[0.47, 2.15]	±40	0.06
Single surface controller K_S (PID)	Break loop at δ_{ac} in Fig. 9	2.5	5.87	[0.5, 2]	±37	20
Single surface controller K_S (H_∞)	Break loop at δ_{ac} in Fig. 9	2.3	4.9	[0.43, 2.3]	±43.4	18

V. Flight Test Results

A. Scope and Overview

The fault-tolerant controller discussed thus far is evaluated by performing autonomous landings (autoland) in the presence of a stuck elevon fault. The scope of the demonstrations is limited as follows. The UAS operator uses a priori knowledge about the airfield and the prevailing winds in order to select the target landing spot. In particular, the aircraft first enters an approach circle and lines up with the runway leading up to this landing spot. Upon exiting the approach circle, the aircraft tracks a glideslope until it reaches a point that is located 100 ft above the target landing spot. At this point, the pilot turns off the fault, takes manual control of the aircraft, and attempts a go-around. Although the autopilot is capable of tracking the glideslope all the way to the ground, it will result in a hard landing. In particular, a final flare is required to rapidly decrease the sink rate and the forward speed of the aircraft prior to touchdown. However, there does not appear to be a way to obtain the final flare using the single control surface, or the throttle, while also maintaining wings-level flight. By taking manual control, the pilot ensures a gentler landing. This reduces the amount of repair work required to prepare the aircraft for the next demonstration. If this were a real-life aborted mission, the hardness of the landing would be immaterial as long as the landing spot is far away from people and property. Further, the demonstrations do not implement a fault diagnosis algorithm. Rather, the fault occurrence triggers the fault-tolerant controller (Fig. 3). The reader is referred to Chapter 6 of [43] for the details on the impact of detection delay on the tolerability of the fault.

A total of six flights are conducted wherein the right elevon is failed at 5° trailing edge up. Table 4 summarizes the flights and indicates whether the PID or the H_∞ controller was used for K_S. The wind speed and direction are from the National Weather Service for KMSP, the weather station closest to the airfield. The battery used in the aircraft provides for a total flight time of around 10 min. On average, the fault tolerant controller is active for about 9 min in each flight. An autoland is attempted, and successfully completed, in four of the six flights. The next section presents one of these flights (FLT35) in detail and Section V.C compares the performance of the fault-tolerant controller in all six flights.

Finally, while the right elevon is failed at $-5°$ in all six flights, any stuck fault for which a steady, wings-level,

constant altitude, and constant airspeed flight condition exists may be tolerated. From a trim analysis, it is estimated that stuck faults that are within $[-7, +5]°$ of the nominal trim elevon position may be tolerated [43].

**Table 4   Summary of flight tests evaluating the fault-tolerant controller.**

| FLT #	Wind speed & direction	K_S design	Active time	Autoland
27	4.5 m/s from SW	PID	9.6 min	Yes
28	6.7 m/s from WWN	PID	9.1 min	Yes
29	6.7 m/s from NW	PID	8.6 min	No
30	6.7 m/s from NW	PID	7.7 min	No
34	2.7 m/s from S	H_∞	8.0 min	Yes
35	2.7 m/s from S	H_∞	9.6 min	Yes

B. One Flight in Detail

FLT35 begins with a manual takeoff, after which the pilot engages the autopilot. Figure 15 shows the ground track of the aircraft from the autopilot engagement (∗) until the landing on the virtual runway (○). The ground track is plotted in a local North-East reference frame whose origin coincides with the target landing spot chosen by the UAS operator. The autopilot engagement (∗) activates the nominal controller, which takes the aircraft into a left banked circle hold at an altitude of 250 ft AGL, an airspeed of 15.4 m/s, and a turn radius of 150 m. The center of the circle $(-120, 6.5)$ m is automatically set by the flight computer to the point where the aircraft climbs past the altitude of 150 ft AGL. This initial phase, wherein the nominal controller is active, is denoted by the dashed line starting at ∗ in Fig. 15. The circle direction (counterclockwise in Fig. 15) depends on the elevon that is faulted, e.g. left banked turns are preferred when the right elevon is faulted and vice-versa. At 945 s, the UAS operator injects a $-5°$ stuck fault in the right elevon (✕), which activates the fault-tolerant controller. The ground track following the fault injection (✕) is denoted using the solid line. For the next 8.2 min, the aircraft performs a circle hold, with a cross-track error standard deviation of 2.9 m.

At 1438 s, the UAS operator initiates the autoland sequence (+) causing the aircraft to peel away from the circle hold and fly towards the approach circle. The location and the radius (100 m in this flight) of the approach circle are selected to avoid obstacles such as trees and poles. The prevailing winds on that day are 2.7 m/s from the South. Although headwind landings are preferred in general, the airfield is shorter along the North-South direction. Thus the operator commands a Westerly landing in this particular flight. The aircraft enters the approach circle (△) and traverses about three-quarters of the circle. Once the aircraft is heading due West, it exits the circle and transitions to glideslope tracking (□). The remainder of the autoland is best explained by the next figure.

Figure 16 shows the terminal flight path of the aircraft as seen by an observer standing on the ground and facing due North. The aircraft tracks a $6°$ glideslope that intersects the virtual runway at an East position of zero. The glideslope tracking is achieved by decreasing h_{cmd} continuously. As discussed in Section III.A, although the phugoid mode is
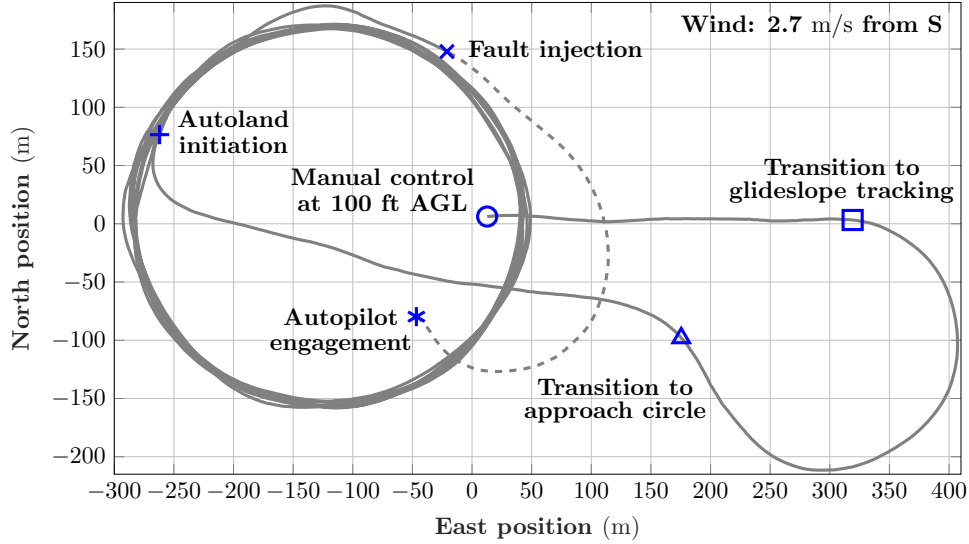
Fig. 15 FLT35: The ground track of the aircraft annotated with the flight events. The fault-tolerant controller is active along the solid line.
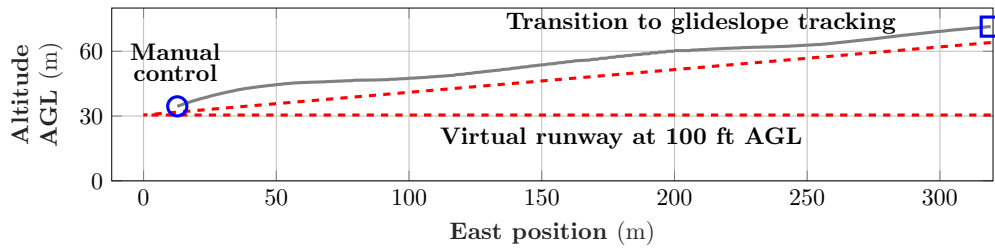

Fig. 16 FLT35: The final approach and landing on the virtual runway.

well-damped, the altitude and the airspeed exhibit steady-state errors. In particular, the new trim airspeed of 14.4 m/s is 1 m/s below its commanded value. This is a constraint imposed by the stuck right elevon. The total energy controller compensates by increasing the altitude by about 5 m above its reference value, as seen in Fig. 16. As explained in Section V.A, the pilot takes manual control of the aircraft (∘) once it reaches 100 ft AGL and performs a go-around (not shown), which terminates with a gentle landing[†].

Figure 17 shows the control commands and the aircraft response immediately after the fault injection. The longitudinal motion variables are close to their respective reference commands and the trim value of the right elevon is approximately $-2°$ before the fault. The fault ($-5°$) causes the aircraft to pitch nose-up to about $25°$ at 949 s. This in turn decreases the airspeed to about 10.2 m/s and increases the altitude by about 32 m. Since the altitude tracking error is much larger than the airspeed tracking error, the fault-tolerant total energy controller decreases the throttle from 0.73 to 0.56. Around 980 s, the airspeed and the pitch angle return closer to their respective reference commands. Since the pitch angle is an uncontrolled variable (Section II.D), its reference command is simply set equal to the trim pitch

---

[†]A video of the autoland taken from an on-board camera is available at: `https://youtu.be/rGIw71kiu4w`

angle. As for the lateral-directional motion variables, the fault causes the aircraft to momentarily roll rightward, as seen between 945 s and 950 s. The single surface controller corrects this by temporarily deflecting the left elevon to $-12°$.
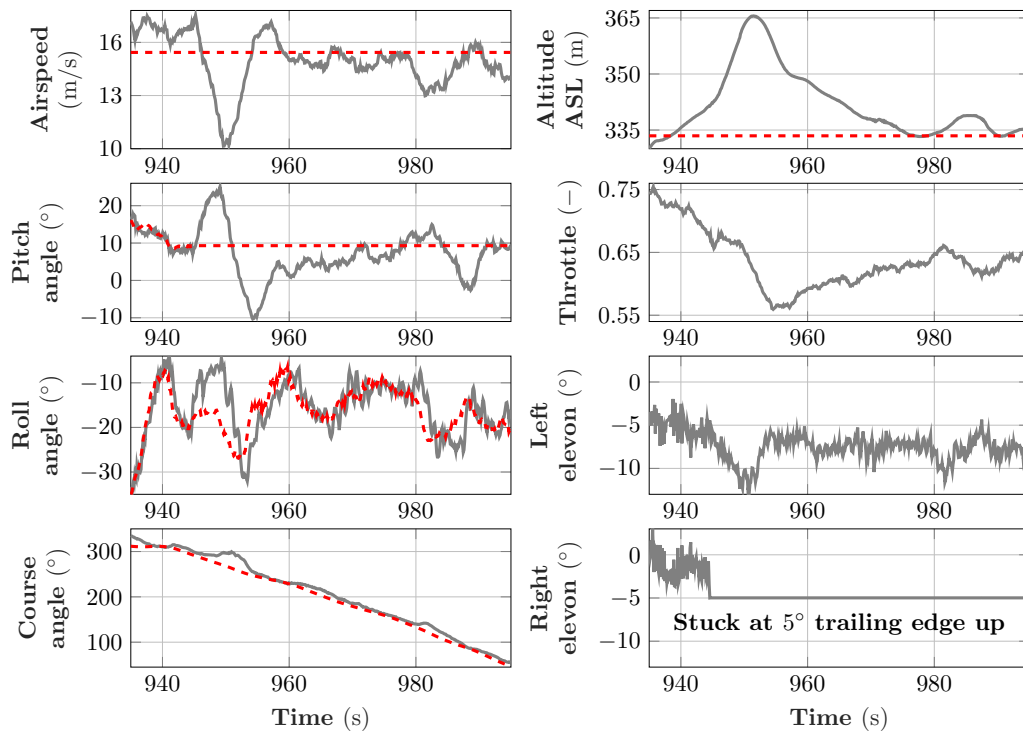

Fig. 17   FLT35: The aircraft response after the fault injection at 945 s.

C. Comparison of All the Flights

Figure 18 shows the three-dimensional trajectories of the four flights that include an autoland (Table 4). Each flight trajectory is shown from the fault injection (✕) until the landing (○) and is plotted in a local East-North-Up reference frame, whose origin coincides with the target landing spot. The dashed lines indicate the glideslope and the virtual runway. As seen in the plots, FLT34 and FLT35 exhibit better tracking during the circle hold and the glideslope phases. This is explained by the better controller (H_∞) used, and the calmer winds observed, during FLT34 and FLT35.

Figure 19 compares the six flights (Table 4) using the summary statistics of the closed-loop tracking errors during the circle hold. The statistics are displayed using box plots for six motion variables. The box plots show the median (black circle), the 25th percentile (lower edge of box), and the 75th percentile (upper edge of box) of the tracking errors before and after the fault injection. For both the pre- and post-fault cases, the statistics are computed over a time segment after the closed-loop has converged to a steady-state. Thus the median is representative of the steady-state tracking error and the interquartile range is representative of the variance in the error. Figure 19 shows that the pre-fault airspeed command is achieved within a steady-state error of ±0.5 m/s in all the flights except FLT35. Although it may appear as such, FLT35 is not an anomaly because the fault is injected before the aircraft reaches its target altitude.
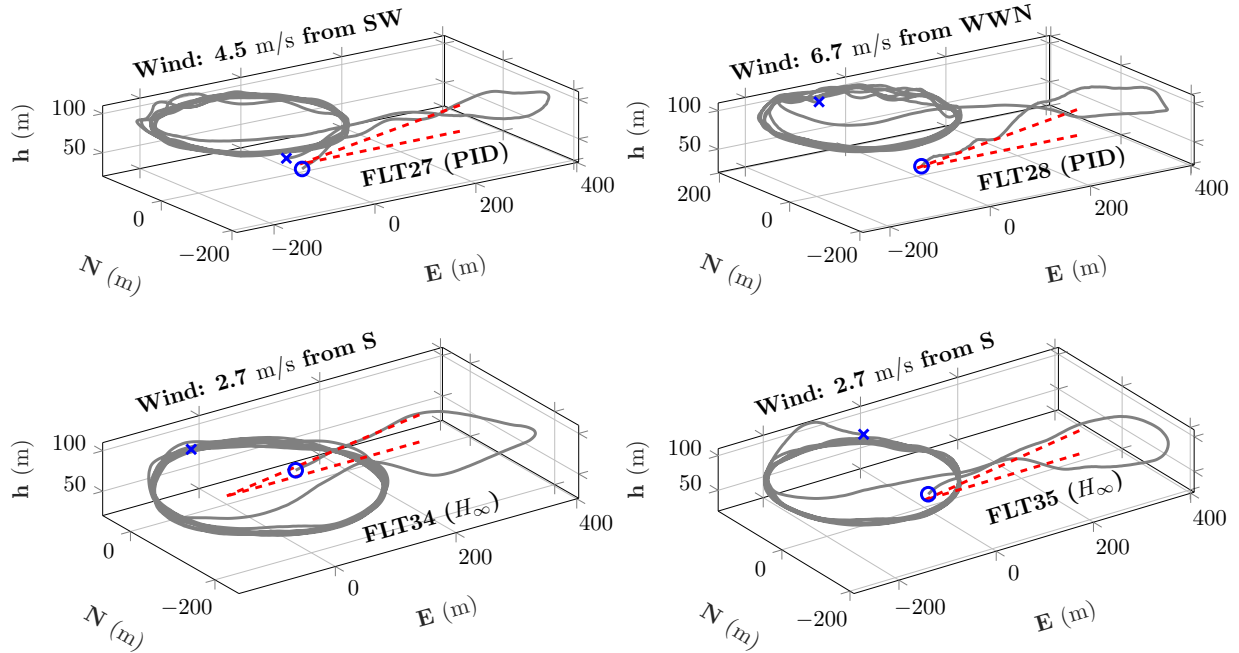
Fig. 18   Three-dimensional views of the flight trajectories during the autoland.

Although the flights share the same fault mode, they have slightly different trim elevon deflections before the fault due to variations in the mass and center of gravity location. In particular, all the flights except FLT34 experience a net trailing edge up deflection of the right elevon after the fault, which causes the trim airspeed to decrease and the trim pitch angle to increase. The relative difference between the nominal and the faulty elevon positions also affects the relative change in the trim airspeed. For example, FLT29 and FLT30 experience small elevon changes and thus small airspeed changes. Further, as explained previously, the airspeed and the altitude exhibit non-zero steady-state errors after the fault injection.

The pre-fault interquartile ranges for a given variable are largely similar across all flights. In addition, the interquartile ranges increase, as expected, after the fault injection. These increases appear to be functions of: the prevailing winds, the controller used, and the variables under consideration. In particular, the longitudinal (airspeed, altitude, and pitch angle) errors appear to be strong functions of the prevailing winds but weak functions of the controller used. For example, FLT28, FLT29, and FLT30 experience high winds (6.7 m/s) and thus exhibit larger longitudinal errors when compared to FLT27 (4.5 m/s). On the other hand, comparing FLT27 with FLT34 and FLT35, both of which also experience moderate winds, reveals that Design B has very little impact in reducing the longitudinal tracking errors. This is because the single surface controller does not directly control any of the longitudinal variables (Section III.B).

The lower output sensitivity of Design B (Fig. 14) translates into better lateral-directional tracking performance. In particular, FLT34 and FLT35 exhibit smaller tracking errors in the roll angle, the course angle, and the cross track when
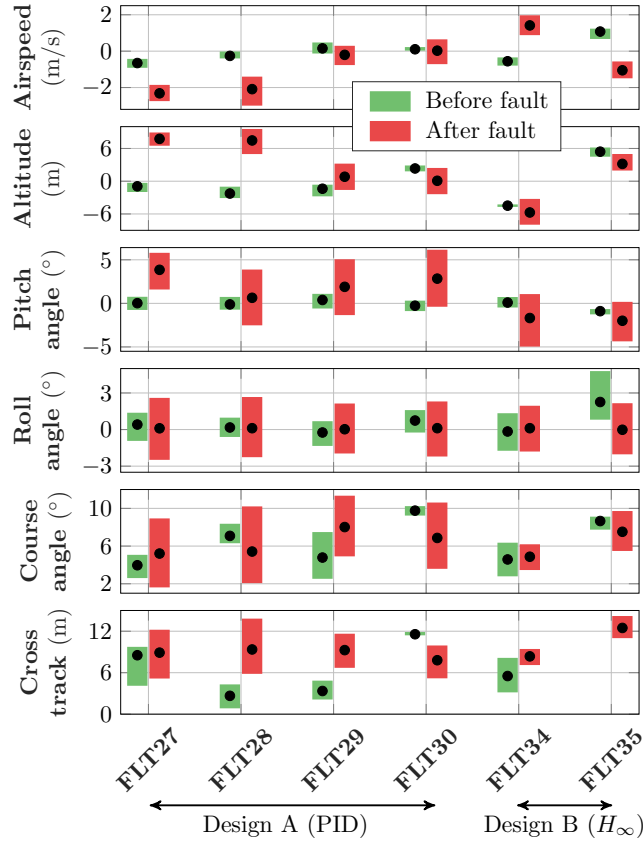
Fig. 19   The summary statistics of the closed-loop tracking errors during the circle hold.

compared to the other flights. While the prevailing winds also affect the lateral-directional tracking errors, they do not seem to be the dominating factor. For example, the course angle error and the cross track error in FLT27 are much higher than those in FLT34 and FLT35 despite the winds being only marginally higher. Further, Design B in some cases yields tracking errors that are on par with those observed before the fault. For example, in FLT34 the interquartile ranges in the course angle error and the cross track error are 3.6° and 5 m pre-fault and 2.7° and 2.3 m post-fault. A similar analysis of closed-loop tracking errors during the glideslope phase of the autoland can be found in Chapter 7 of [43]. The flight tests corroborate the comparisons drawn between the PID and H_∞ controllers in Section IV.A.

VI. Conclusions

This paper considers the problem of controlling a small unmanned aircraft using only one of its elevons and the throttle. Since the aircraft is under-actuated, the throttle is used for total energy control and the single elevon is used for lateral control. While this strategy sacrifices longitudinal tracking performance, the fault-tolerant control design ensures that the phugoid and the short period modes have favorable properties. The operable elevon is controlled using either a PID or an H_∞ controller. The fault-tolerant controller is evaluated by performing autonomous landings in the presence

of a stuck elevon fault. The H_∞ controller is more robust and yields better tracking performance during the flight tests. In addition, the H_∞ controller actuates the single operable elevon only in the frequency range required for lateral control and does not excite the short period mode. These are direct consequences of incorporating weights that penalize the input/output disturbances and excessive control effort in the H_∞ synthesis.

Appendix

The matrices listed consider all the signals in SI units. The state-space matrices of the longitudinal model G_{lon} are:

$$
\mathbf{A_{lon}} = \begin{bmatrix} -0.151 & 0.753 & -1.02 & -9.78 & 0 \\ -0.883 & -5.69 & 13.9 & -0.668 & 0 \\ 0.878 & -12.9 & -5.49 & 0 & 0 \\ 0 & 0 & 1 & 0 & 0 \\ -0.0681 & 0.998 & 0 & -15.4 & 0 \end{bmatrix}, \ \mathbf{B_{lon}} = \begin{bmatrix} 6.53 & 0.146 \\ 0 & -24.5 \\ 0 & -186 \\ 0 & 0 \\ 0 & 0 \end{bmatrix}, \ \mathbf{C_{lon}} = \begin{bmatrix} 0.998 & 0.0681 & 0 & 0 & 0 \\ 0 & 0 & 1 & 0 & 0 \\ 0 & 0 & 0 & 1 & 0 \\ 0 & 0 & 0 & 0 & -1 \end{bmatrix}, \ \text{and } \mathbf{D_{lon}} = \begin{bmatrix} 0 & 0 \\ 0 & 0 \\ 0 & 0 \\ 0 & 0 \end{bmatrix}. \quad (16)
$$

The state-space matrices of the lateral-directional model G_{lat} are:

$$
\mathbf{A_{lat}} = \begin{bmatrix} -0.574 & 1.12 & -15.3 & 9.78 \\ -3.99 & -11.3 & 2.5 & 0 \\ 0.311 & -1.49 & -0.944 & 0 \\ 0 & 1 & 0.0683 & 0 \end{bmatrix}, \ \mathbf{B_{lat}} = \begin{bmatrix} -0.488 \\ -201 \\ -9.61 \\ 0 \end{bmatrix}, \ \mathbf{C_{lat}} = \begin{bmatrix} 0 & 0 & 0 & 1 \\ 0 & 1 & 0 & 0 \end{bmatrix}, \ \text{and } \mathbf{D_{lat}} = \begin{bmatrix} 0 \\ 0 \end{bmatrix}. \quad (17)
$$

G_t^P is obtained by replacing the delay in $G_t e^{-\tau_f s}$ with a second-order Padé approximation. The delay in $G_a e^{-\tau_f s}$ is first replaced with a fifth-order Padé approximation. A balanced residualization [49] of two states yields G_a^L.

The model G_f for a stuck right elevon has the state-space representation:

$$
\mathbf{A} = \begin{bmatrix} 0 & 0 & 1 & 0 & 0.068 & 0 & 0 & 0 & 0 \\ 0 & 0 & 0 & 1 & 0 & 0 & 0 & 0 & 0 \\ 0 & 0 & -11 & 0 & 2.5 & 0 & -3.99 & 0 & 0 \\ 0 & 0 & 0 & -5.49 & 0 & 0.88 & 0 & -12.9 & 0 \\ 0 & 0 & -1.5 & 0 & -0.944 & 0 & 0.311 & 0 & 0 \\ 0 & -9.78 & 0 & -1.02 & 0 & -0.15 & 0 & 0.753 & 0 \\ 9.78 & 0 & 1.12 & 0 & -15.3 & 0 & -0.573 & 0 & 0 \\ 0 & -0.67 & 0 & 13.9 & 0 & -0.88 & 0 & -5.69 & -9.43e{-}4 \\ 0 & -15.4 & 0 & 0 & 0 & -0.068 & 0 & 0.998 & 0 \end{bmatrix}, \ \mathbf{B} = \begin{bmatrix} 0 & 0 \\ 0 & 0 \\ 0 & 100 \\ 0 & -92.9 \\ 0 & 4.81 \\ 6.53 & 0.073 \\ 0 & 0.244 \\ 0 & -12.3 \\ 0 & 0 \end{bmatrix}, \ \mathbf{C} = \begin{bmatrix} 0 & 0 & 0 & 0 & 0 & 0.99 & 0 & 0.07 & 0 \\ 0 & 0 & 0 & 0 & 0 & 0 & 0 & 0 & -1 \\ 1 & 0 & 0 & 0 & 0 & 0 & 0 & 0 & 0 \\ 0 & 1 & 0 & 0 & 0 & 0 & 0 & 0 & 0 \\ 0 & 0 & 1 & 0 & 0 & 0 & 0 & 0 & 0 \\ 0 & 0 & 0 & 1 & 0 & 0 & 0 & 0 & 0 \\ 0 & 0 & 0 & 0 & 1 & 0 & 0 & 0 & 0 \end{bmatrix}, \ \mathbf{D} = 0_{7\times2}.
$$

$$(18)$$

The state-space matrices of the eighth-order continuous-time controller K_A are:

$$
\mathbf{A_K} = \begin{bmatrix} 0 & 0 & 0 & 0 & 0 & 0 & 0 & 0 \\ 0 & -5.39 & 4.54 & 4.55 & 12.4 & -1.19 & 6.65 & 0.93 \\ 0 & 3.55 & -4.3 & -15 & -31.3 & 1.6 & -10.07 & -1.36 \\ 0 & -4.46 & 14.9 & -2.27 & -8.29 & 3.24 & -8.04 & -1.25 \\ 0 & -12.4 & 30.3 & -5.5 & -21.8 & 13.5 & -26.9 & -4.25 \\ 0 & -1.19 & 1.15 & -3.16 & -13.5 & -0.713 & 8.17 & 0.962 \\ 0 & -6.56 & 9.66 & -8.01 & -26.4 & -7.94 & -118 & -48.5 \\ 0 & 0.896 & -1.33 & 1.25 & 4.1 & 0.890 & 48.3 & -7.99 \end{bmatrix}, \ \mathbf{B_K} = \begin{bmatrix} -9.7 & 9.7 & 0 \\ 1.12 & -1.12 & -0.338 \\ -0.485 & 0.485 & 0.55 \\ 0.329 & -0.329 & -0.233 \\ 1.02 & -1.02 & -0.293 \\ 0.141 & -0.141 & -0.0212 \\ 0.647 & -0.647 & -0.362 \\ -0.0882 & 0.0882 & 0.0647 \end{bmatrix},
$$

$$
\mathbf{C_K} = \begin{bmatrix} 0.00852 & -1.62 & 0.879 & 0.52 & 1.48 & -0.2 & 0.984 & 0.141 \end{bmatrix}, \ \mathbf{D_K} = \begin{bmatrix} -0.000442 & 0.000442 & -0.000101 \end{bmatrix}. \quad (19)
$$

Funding Sources

Acknowledgments

References

[1] Freeman, P., "Reliability Assessment for Low-cost Unmanned Aerial Vehicles," Ph.D. thesis, University of Minnesota, 2014.

[2] Chen, J., and Patton, R. J., *Robust Model-Based Fault Diagnosis for Dynamic Systems*, Springer, Boston, MA, 1999, Chap. 1. doi:10.1007/978-1-4615-5149-2.

[3] Isermann, R., *Fault-Diagnosis Systems: An Introduction from Fault Detection to Fault Tolerance*, Springer, Germany, 2006, Chaps. 18,19. doi:10.1007/3-540-30368-5.

[4] Ding, S. X., *Data-driven Design of Fault Diagnosis and Fault-tolerant Control Systems*, Springer-Verlag, 2014, Chaps. 13, 14, 15. doi:10.1007/978-1-4471-6410-4.

[5] Blanke, M., Kinnaert, M., Lunze, J., and Staroswiecki, M., *Diagnosis and Fault-Tolerant Control*, Springer-Verlag, 2016, Chaps. 8, 9, 10. doi:10.1007/978-3-662-47943-8.

[6] Hajiyev, C., and Caliskan, F., *Fault Diagnosis and Reconfiguration in Flight Control Systems*, Springer-Verlag, 2003, Chap. 10. doi:10.1007/978-1-4419-9166-9.

[7] Edwards, C., Lombaerts, T., and Smaili, H. (eds.), *Fault Tolerant Flight Control: A Benchmark Challenge*, Springer-Verlag, 2010, Chaps. 2, 5, 6. doi:10.1007/978-3-642-11690-2.

[8] Steinberg, M., "Historical Overview of Research in Reconfigurable Flight Control," *Journal of Aerospace Engineering*, Vol. 219, No. 4, 2005, pp. 263–275. doi:10.1243/095441005X30379.

[9] Zhang, Y., and Jiang, J., "Bibliographical review on reconfigurable fault-tolerant control systems," *Annual Reviews in Control*, Vol. 32, No. 2, 2008, pp. 229–252. doi:10.1016/j.arcontrol.2008.03.008.

[10] Stewart, J. F., and Shuck, T. L., "Flight-testing of the self-repairing flight control system using the F-15 highly integrated digital electronic control flight research facility," Tech. rep., NASA, 1990. NASA-TM-101725.

[11] Burken, J., Maine, T., Burcham, Jr., F., and Kahler, J., "Longitudinal emergency control system using thrust modulation demonstrated on an MD-11 airplane," *32nd AIAA/ASME/SAE/ASEE Joint Propulsion Conference*, 1996. doi:10.2514/6.1996-3062, AIAA Paper 1996-3062.

[12] Yu, X., Liu, Z., and Zhang, Y., "Fault-Tolerant Flight Control Design With Finite-Time Adaptation Under Actuator Stuck Failures," *IEEE Transactions on Control Systems Technology*, Vol. 25, No. 4, 2017, pp. 1431–1440. doi:10.1109/TCST.2016.2603072.

[13] Pachter, M., and Huang, Y., "Fault Tolerant Flight Control," *Journal of Guidance, Control, and Dynamics*, Vol. 26, No. 1, 2003, pp. 151–160. doi:10.2514/2.5026.

[14] Nguyen, N., Krishnakumar, K., and Kaneshige, J., "Flight Dynamics and Hybrid Adaptive Control of Damaged Aircraft," *Journal of Guidance, Control, and Dynamics*, Vol. 31, No. 3, 2008, pp. 751–764. doi:10.2514/1.28142.

[15] Jourdan, D., Piedmonte, M., Gavrilets, V., Vos, D., and McCormick, J., "Enhancing UAV Survivability Through Damage Tolerant Control," *AIAA Guidance, Navigation, and Control Conference*, 2010. doi:10.2514/6.2010-7548, AIAA Paper 2010-7548.

[16] Chowdhary, G., Johnson, E. N., Chandramohan, R., Kimbrell, M. S., and Calise, A., "Guidance and Control of Airplanes Under Actuator Failures and Severe Structural Damage," *Journal of Guidance, Control, and Dynamics*, Vol. 36, No. 4, 2013, pp. 1093–1104. doi:10.2514/1.58028.

[17] Shore, D., and Bodson, M., "Flight Testing of a Reconfigurable Control System on an Unmanned Aircraft," *Journal of Guidance, Control, and Dynamics*, Vol. 28, No. 4, 2005, pp. 698–707. doi:10.2514/1.8178.

[18] Maciejowski, J. M., and Jones, C. N., "MPC fault-tolerant flight control case study: Flight 1862," *IFAC Proceedings Volumes*, Vol. 36, No. 5, 2003, pp. 119–124. doi:10.1016/S1474-6670(17)36480-7.

[19] Monaco, J., Ward, D., Barron, R., and Bird, R., "Implementation and flight test assessment of an adaptive, reconfigurable flight control system," *AIAA Guidance, Navigation, and Control Conference*, 1997. doi:10.2514/6.1997-3738, AIAA Paper 1997-3738.

[20] Page, A., Monaco, J., and Meloney, D., "Flight Testing of a Retrofit Reconfigurable Control Law Architecture Using an F/A-18C," *AIAA Guidance, Navigation, and Control Conference*, 2006. doi:10.2514/6.2006-6052, AIAA Paper 2006-6052.

[21] Ward, D. G., Monaco, J. F., and Bodson, M., "Development and Flight Testing of a Parameter Identification Algorithm for Reconfigurable Control," *Journal of Guidance, Control, and Dynamics*, Vol. 21, No. 6, 1998, pp. 948–956. doi:10.2514/2.4329.

[22] Cieslak, J., Henry, D., Zolghadri, A., and Goupil, P., "Development of an Active Fault-Tolerant Flight Control Strategy," *Journal of Guidance, Control, and Dynamics*, Vol. 31, No. 1, 2008, pp. 135–147. doi:10.2514/1.30551.

[23] Hitachi, Y., "Damage-Tolerant Control System Design for Propulsion-Controlled Aircraft," Master's thesis, University of Toronto, 2009.

[24] Bennani, S., van der Sluis, R., Schram, G., and Mulder, J., "Control law reconfiguration using robust linear parameter varying control," *AIAA Guidance, Navigation, and Control Conference*, 1999. doi:10.2514/6.1999-4137, AIAA Paper 1999-4137.

[25] Ganguli, S., Marcos, A., and Balas, G., "Reconfigurable LPV control design for Boeing 747-100/200 longitudinal axis," *American Control Conference*, 2002, pp. 3612–3617. doi:10.1109/ACC.2002.1024489.

[26] Zhong, L., and Mora-Camino, F., "On-line Optimization for Fault Tolerant Flight Control," *Procedia Engineering*, Vol. 80, 2014, pp. 638–655. doi:10.1016/j.proeng.2014.09.119.

[27] Ducard, G. J. J., "Fault-Tolerant Flight Control and Guidance Systems for a Small Unmanned Aerial Vehicle," Ph.D. thesis, ETH Zurich, 2007. doi:10.3929/ethz-a-005582839.

[28] Brinker, J. S., and Wise, K. A., "Flight Testing of Reconfigurable Control Law on the X-36 Tailless Aircraft," *Journal of Guidance, Control, and Dynamics*, Vol. 24, No. 5, 2001, pp. 903–909. doi:10.2514/2.4826.

[29] Schierman, J., Ward, D., Hull, J., Gandhi, N., Oppenheimer, M., and Doman, D., "Integrated Adaptive Guidance and Control for Re-Entry Vehicles with Flight Test Results," *Journal of Guidance, Control, and Dynamics*, Vol. 27, No. 6, 2004, pp. 975–988. doi:10.2514/1.10344.

[30] Lombaerts, T. J. J., "Fault Tolerant Flight Control: A Physical Model Approach," Ph.D. thesis, TU Delft, 2010.

[31] Chandler, P. R., Pachter, M., and Mears, M., "System identification for adaptive and reconfigurable control," *Journal of Guidance, Control, and Dynamics*, Vol. 18, No. 3, 1995, pp. 516–524. doi:10.2514/3.21417.

[32] Bobrow, J. E., and Murray, W., "An algorithm for RLS identification of parameters that vary quickly with time," *IEEE Transactions on Automatic Control*, Vol. 38, No. 2, 1993, pp. 351–354. doi:10.1109/9.250491.

[33] Ward, D. G., Barron, R. L., Carley, M. P., and Curtis, T. J., "Real-time parameter identification for self-designing flight control," *NAECON*, 1994, pp. 526–531. doi:10.1109/NAECON.1994.332860.

[34] Bodson, M., "An adaptive algorithm with information-dependent data forgetting," *American Control Conference*, 1995, pp. 3485–3489. doi:10.1109/ACC.1995.533784.

[35] Boskovic, J. D., Prasanth, R., and Mehra, R. K., "Retrofit Fault-Tolerant Flight Control Design Under Control Effector Damage," *Journal of Guidance, Control, and Dynamics*, Vol. 30, No. 3, 2007, pp. 703–712. doi:10.2514/1.25564.

[36] Handelman, D. A., and Stengel, R. F., "Combining expert system and analytical redundancy concepts for fault-tolerant flight control," *Journal of Guidance, Control, and Dynamics*, Vol. 12, No. 1, 1989, pp. 39–45. doi:10.2514/3.20366.

[37] Shuang, W., Zhang, S., Wu, X., Van Kampen, E. J., and Chu, Q. P., "An Anti-windup Fault Tolerant Control Scheme with Guaranteed Transient Performance for Tailless Flying Wing Aircraft," *AIAA Guidance, Navigation, and Control Conference*, 2017. doi:10.2514/6.2017-1253, AIAA Paper 2017-1253.

[38] Tang, X., Tao, G., and Joshi, S. M., "Adaptive actuator failure compensation for nonlinear MIMO systems with an aircraft control application," *Automatica*, Vol. 43, No. 11, 2007, pp. 1869–1883. doi:10.1016/j.automatica.2007.03.019.

[39] Tao, G., "Direct adaptive actuator failure compensation control: a tutorial," *Journal of Control and Decision*, Vol. 1, No. 1, 2014, pp. 75–101. doi:10.1080/23307706.2014.885292.

[40] Venkataraman, R., and Seiler, P., "Safe Flight Using One Aerodynamic Control Surface," *AIAA Guidance, Navigation, and Control Conference*, 2016. doi:10.2514/6.2016-0634, AIAA Paper 2016-0634.

[41] Venkataraman, R., Seiler, P., and Taylor, B., "Fault-tolerant aircraft flight control using a subset of aerodynamic control surfaces," United States Patent Application US 2017/0349267 A1, May 2017.

[42] Krause, A., Condron, R., Day, E., Dessens, D., and Wagner, P., "Single Control Surface UAV," Tech. rep., University of Minnesota, 2016.

[43] Venkataraman, R., "Fault-Tolerant Flight Control Using One Aerodynamic Control Surface," Ph.D. thesis, University of Minnesota, 2018.

[44] Cook, M. V., *Flight Dynamics Principles*, 2nd ed., Elsevier, 2007, Chaps. 4,6. doi:10.1016/B978-0-7506-6927-6.X5000-4.

[45] Nelson, R. C., *Flight Stability and Automatic Control*, McGraw-Hill, 1998, Chaps. 3, 5.

[46] Park, S., Deyst, J., and How, J., "Performance and Lyapunov Stability of a Nonlinear Path-Following Guidance Method," *Journal of Guidance, Control, and Dynamics*, Vol. 30, No. 6, 2007, pp. 1718–1728. doi:10.2514/1.28957.

[47] Liberzon, D., *Switching in Systems and Control*, Birkhauser Basel, 2003, Chaps. 1, 2, 3, 5. doi:10.1007/978-1-4612-0017-8.

[48] Yang, H., Jiang, B., and Staroswiecki, M., "Supervisory fault tolerant control for a class of uncertain nonlinear systems," *Automatica*, Vol. 45, No. 10, 2009, pp. 2319–2324. doi:10.1016/j.automatica.2009.06.019.

[49] Skogestad, S., and Postlethwaite, I., *Multivariable Feedback Control: Analysis and Design*, Wiley, 2005, Chaps. 2, 5, 9, 11.

[50] Lambregts, A. A., "Vertical flight path and speed control autopilot design using total energy principles," *AIAA Guidance, Navigation, and Control Conference*, 1983. doi:10.2514/6.1983-2239, AIAA Paper 1983-2239.

[51] Lambregts, A. A., "Integrated system design for flight and propulsion control using total energy principles," *AIAA Aircraft Design, Systems, and Technology Meeting*, 1983. doi:10.2514/6.1983-2561, AIAA Paper 1983-2561.

[52] Beard, R. W., "Total Energy Control for Longitudinal Autopilot," , October 2014. Book supplement to Small Unmanned Aircraft.

[53] Doyle, J., Glover, K., Khargonekar, P., and Francis, B., "State-space solutions to standard H_2 and H_∞ control problems," *IEEE Transactions on Automatic Control*, Vol. 34, No. 8, 1989, pp. 831–847. doi:10.1109/9.29425.